Solar Energy 164 (2018) 160–173

Contents lists available at ScienceDirect

Solar Energy

journal homepage: www.elsevier.com/locate/solener

# Optical losses of photovoltaic modules due to mineral dust deposition: Experimental measurements and theoretical modeling

Patricio G. Piedra[a,b,*], Laura R. Llanza[a,1], Hans Moosmüller[a]

[a] Laboratory for Aerosol Science, Spectroscopy, and Optics, Desert Research Institute, Nevada System of Higher Education, 2215 Raggio Parkway, Reno, NV 89512, USA
[b] U.S. Army Research Laboratory, 2800 Powder Mill Road, Adelphi, MD 20783, USA

ARTICLE INFO

*Keywords:*
Radiative transfer
Photovoltaic modules
Soiling
Two stream theory

ABSTRACT

Deposition of particles on photovoltaic (PV) modules has the potential to increase costs of solar energy production and maintenance and to affect grid-connected energy forecasting. Particles deposited on PV modules can reduce the optical transmission to the PV semiconductor significantly (>50%) due to absorption and scattering. Although there are many previous studies of PV module efficiency losses with respect to exposure time, angle tilt of the PV module, and other environmental factors, there has been little study of PV module efficiency losses with respect to the optical characteristics of the deposited particles (e.g., refractive index, optical depth). Here, we deposited two types of dust onto glass slides, optically absorbing dust and optically non-absorbing dust. We systematically increased the mass per unit area deposited onto the glass slides and measured the optical depth and total transmission (i.e., direct plus diffuse light) using a spectrophotometer with an integrating sphere detector system. Our experimental measurements were compared with a two-stream radiative transfer model, and with Monte Carlo radiative transfer calculations, yielding good agreement for both absorbing and non-absorbing dust. Our results indicate that total transmission decreases approximately linearly as a function of dust mass deposited per unit area, with the slope being highly sensitive to the absorptivity of the dust. The obtained results and models used in this study can be used in conjunction with deposition models to predict the degradation of the optical transmission of PV modules with respect to mass per unit area dust loading.

## 1. Introduction

Solar photovoltaic (PV) modules are exposed to the environment, and aerosol particles, including mineral dust, can deposit on them. Experimental studies have revealed that dust deposition can significantly (> 50%) degrade the power output of PV modules (Sayyah et al., 2014; Sulaiman et al., 2014). These deposited particles cause output power losses for the PV module due to reduced irradiance interacting with the PV module semiconductor, and we shall henceforth refer to these optical losses simply as efficiency losses. Although some experimental work on PV module efficiency losses as a function of environmental factors (e.g., exposure time, wind speed, relative humidity, PV module tilt angle) has been done (Etyemezian et al., 2017; Maghami et al., 2016; Mani and Pillai, 2010), very few experiments have studied PV module efficiency losses as a function of deposited aerosol optical depth $\tau_0$, the key parameter quantifying optical transmission through a layer of particles. In recent years, there has been growing interest in reducing solar energy costs in order to compete with energy generated from fossil fuels. For this reason, one of the important current goals of the U.S. Department of Energy is the reduction of cost of PV solar energy to ~$0.08 per kilowatt-hour (Fu et al., 2017). Similarly, there has been growing interest in energy forecasting given the increasing penetration of grid-connected solar power (Inman et al., 2013). One important factor influencing solar energy costs as well as solar energy forecasting is the reduced efficiency of PV modules with particle deposits on their surfaces (Costa et al., 2017; Gholami et al., 2017). Deposited aerosol particles extinguish irradiance directed towards the PV semiconductor due to scattering and absorption (Moosmüller et al., 2009), but mathematical modeling of these mechanisms is lacking. Among one of the very few modeling studies, Al-Hasan (1998) developed a model for reduction of transmission of direct radiation onto a PV module, with experimental validity of up to 50% transmission reduction. Building on this work, there have been recent studies modeling direct transmission reduction for PV modules with low soiling loadings on the order of ~0.2 g/m$^2$ (Sun et al., 2017). Similarly, our group has conducted a theoretical study of the optical losses due to scattering and absorption of radiation by particles deposited onto PV modules. This previous study (Piedra and Moosmüller,

* Corresponding author at: U.S. Army Research Laboratory, 2800 Powder Mill Road, Adelphi, MD 20783, USA.
*E-mail address:* patricio.piedracartagena.ctr@mail.mil (P.G. Piedra).
[1] Now at Facultat de Matemàtiques i Informàtica, Universitat de Barcelona, Barcelona, Catalonia, Spain.

https://doi.org/10.1016/j.solener.2018.02.030
Received 29 September 2017; Received in revised form 9 February 2018; Accepted 9 February 2018

2017) considered that optical losses are fundamentally due to scattering into the backward hemisphere direction and due to absorption, but that forward hemisphere scattering still reaches the PV semiconductor. This work was limited to small ($\tau_0 \ll 1$) optical depths of deposited aerosol and did not include any comparison with experimental results. In addition, we do not know of any models of PV module efficiency losses as a function of optical depth that consider both the direct beam (defined here as the part of the transmitted solar radiation unaffected by deposited dust) as well as the diffuse radiation (defined here as the part of the transmitted solar radiation scattered by deposited dust).

Here, we develop an optical model based on the two-stream approximation (Bohren, 1987) to calculate the optical losses due to deposition of aerosols onto PV modules that includes direct and diffuse radiation. In addition, we present calculations of optical losses using Monte Carlo techniques (e.g., Wang et al., 1995). The validity of our models is examined by experimentally depositing suspended dust onto glass slides acting as surrogates for PV modules. The models presented here assume normally-incident, monochromatic light. They can be expanded to different incidence angles by discretization of directionality, for instance by the discrete-ordinate method (Liou, 2002) and to the spectrum of incident solar radiation by integration over the relevant wavelength region with a spectral sensitivity function for the PV module of interest. These optical models can be used in conjunction with deposition models, relevant to the location of interest, to predict optical efficiency losses of PV modules due to aerosol deposition. The potential use of these models for forecasting applications is described in Section 5. Abbreviations used in this publication are listed in Table 1 in order of appearance.

Similarly, mathematical symbols used are listed in Table 2 in order of appearance.

## 2. Experimental measurements

In the following section, we describe a suspension-deposition experiment that was conducted to suspend mineral dust and subsequently allowing it to settle gravitationally onto glass slides that are used as surrogate for PV module surfaces.

### 2.1. Mineral dust suspension and deposition

We suspended absorbing and non-absorbing mineral dust samples with a mass of ~20 g sample placed into a sample flask. The absorbing dust consisted of pure hematite ($Fe_2O_3$) particles (Powder Technology Inc.). The non-absorbing dust was an off-white lakebed deposit, diatomaceous shale, consisting of plagioclase, quartz, and lesser amounts of clay, collected as part of a recent study on the characterization of mineral dust (Engelbrecht et al., 2016; Moosmüller et al., 2012). Pressurized air was injected into the sample flask, entraining the sample and transporting it through a tube into the deposition chamber where it consequently gravitationally settles and deposits onto glass slides placed horizontally at the bottom of the deposition chamber (see Fig. 1). We systematically increased the amount of mass per unit area $\rho_m$ deposited on our glass slides by increasing the time that pressurized air was injected into the flask. Dust deposited onto the horizontal glass slide. However, for optical characterization of the glass slide plus deposit, the glass slide with deposit had to be rotated into a vertical position. This limited our deposition mass density $\rho_m$ because above a certain mass density, dust would fall off the slide when positioned vertically. The limits observed were $\rho_m \approx 14\ g/m^2$ for the absorbing sample and $\rho_m \approx 9\ g/m^2$ for the non-absorbing sample. These limits are consistent with a PV module's cumulative dust loading over more than 100 days of exposure in Doha, Qatar (Javed et al., 2017). We obtained size distributions for the deposited mineral dust particles from digital image analysis of scanning electron microscope (SEM) images of the deposits. For this analysis, we used dust depositions with nearly equal, low area mass density (i.e., $0.43\ g/m^2$ for non-absorbing dust and $0.44\ g/m^2$ for absorbing dust). The particles' longest dimensional lengths (the "diameter") yielded a histogram that was fitted with a log-normal number size distribution $n(D)$ given by

$$n(D) = \frac{1}{C\sigma D\sqrt{2\pi}} \exp\left[-0.5\left(\frac{\ln D - \mu}{C\sigma}\right)^2\right], \quad (1)$$

where $D$ is a free variable used to represent the longest length of the particles as a continuous probability distribution function, $\sigma$ is the standard deviation of $\ln D$, $\mu$ is the mean of $\ln D$, and $C$ is a scaling constant used to normalize the probability distribution such that the integral of $n(D)$ over the $D$ domain is one. The normalized histograms and curve-fits can be seen in Fig. 2, including its fitting parameters. The peak or mode of the log-normal distribution for the absorbing samples was located at ~1.3 μm, while the peak of the non-absorbing sample was located at ~0.8 μm.

**Table 1**
List of abbreviations used.

| Abbreviation | Meaning |
|---|---|
| PV | Photovoltaic |
| SEM | Scanning Electron Microscope |
| SIS | Spherical Integrating Spectrophotometer |
| AOD | Aerosol Optical Depth |
| SSA | Single Scattering Albedo |

### 2.2. Optical characterization of deposited dust

The optical properties of mineral dust samples deposited on glass slides were characterized with a Perkin Elmer 1050 UV/Vis/NIR spherical integrating spectrophotometer (SIS) equipped with a detector system consisting of a 150-mm diameter integrating sphere with InGaAs/PMT detectors covering the 250 to 2500-nm spectral range (Padera, 2013). This SIS system has two measurement ports: a transmission port located in front of the sphere, and a reflection port located at the back of the sphere (Figs. 3 and 4). It allows for measuring either the scattering into the forward hemisphere (Fig. 3) or the total transmission into the forward hemisphere, which is the sum of direct beam transmission and scattering into the forward hemisphere (Fig. 4).

We have normalized our measurements of dust-deposited (dirty) glass slides transmission $T$ so that the non-deposited (clean) glass slide transmission $T_{clean\ raw}$ is normalized to $T_{clean} = 1$. The normalized transmission $T_{norm}$ of the particles-glass slide system is obtained from a raw measurement $T_{raw}$ normalized with respect to the raw measurement of a clean glass slide transmission $T_{clean\ raw}$ as

$$T_{norm} = \frac{T_{raw}(\lambda)}{T_{clean\ raw}(\lambda)}. \quad (2)$$

This normalization isolates the effect of deposited dust on optical transmission. In our experiments, $T_{clean\ raw}$ ranged from ~0.91 to ~0.93, comparable to the normal incidence ~0.92 transmission through an air-glass-air system with glass refractive index of 1.5, where losses are caused by Fresnel reflections from two surfaces. All transmission measurements discussed in the following discussion have been normalized with Eq. (2).

#### 2.2.1. Forward-Hemisphere scattering measurement

The SIS spectrometer can be used to selectively measure the transmission of light scattered into the forward hemisphere $T_{fwd}$ by locating the sample in the transmittance port in front of the SIS and eliminating the direct beam power through absorption by a non-reflecting (black) surface (Fig. 3).

**Table 2**
List of mathematical symbols used. If common unit box is blank, the quantity has unit one (i.e., unitless).

| Symbol | Common unit | Meaning |
|---|---|---|
| $\rho_m$ | g/m$^2$ | Mass of dust deposited on glass slide or PV module per unit area |
| $n(D)$ | μm$^{-1}$ | Probability distribution function describing the sample number size distribution |
| $D$ | μm | Longest length of particle as observed by SEM image analysis |
| $C$ | | Normalization constant for particle number size distribution |
| $\mu$ | | Mean of ln$D$ |
| $\sigma$ | | Standard deviation of ln$D$ |
| $\lambda$ | nm | Wavelength |
| $T_{raw}(\lambda)$ | | Non-normalized total transmission of dusty glass slide measured by SIS |
| $T_{clean\ raw}(\lambda)$ | | Non-normalized total transmission of clean glass slide measured by SIS |
| $T_{norm}$ | | Normalized direct and/or diffuse transmission measured by SIS |
| $T_{measured}$ | | Normalized total (i.e., direct plus diffuse) transmission into the forward hemisphere measured by SIS |
| $T_{fwd}$ | | Normalized diffuse transmission into the forward hemisphere measured with SIS by eliminating direct transmission through insertion of a non-reflective substrate into the direct beam |
| $T_{dir}$ | | Direct transmission $T_{dir} = T_{measured} - T_{fwd}$ |
| $P_0$ | W/m$^2$ | Power of monochromatic light beam normal-incident onto glass slide with dust sample |
| $P$ | W/m$^2$ | Power direct transmitted (i.e., unaffected by interactions with dust on glass slide with dust sample) |
| $\tau_0$ | | Optical depth of dust sample |
| $\tau_0'$ | | Scaled optical depth of dust sample retrieved by SIS measurement |
| $\tau$ | | Optical depth as a mathematical variable |
| $f$ | | Fraction of diffuse power transmitted into the near-forward direction and truncated by SIS configuration |
| $\bar{\omega}$ | | Single scattering albedo of dust sample |
| $g$ | | Asymmetry parameter of dust sample |
| $m$ | | Complex refractive index of dust |
| $m_r$ | | Real part of the refractive index of dust |
| $m_i$ | | Imaginary part of the refractive index of dust |
| $P_\downarrow$ | W/m$^2$ | Optical power per area transmitted into the direction normally towards PV semiconductor |
| $P_\uparrow$ | W/m$^2$ | Optical power per area transmitted into the direction normally away from PV semiconductor |
| $K$ | | $K \equiv \sqrt{(1-\bar{\omega})(1-\bar{\omega}g)}$ |
| $T$ | | Total direct and diffuse transmittance modeled by two-stream theory |
| $\sigma_{sca}$ | μm$^2$ | Scattering cross section of dust |
| $\sigma_{ext}$ | μm$^2$ | Extinction cross section of dust |
| $\frac{d\sigma_{sca}}{d\Omega}$ | μm$^2$/Sr | Differential scattering cross section into solid angle $d\Omega$ |
| $\theta$ | Radian | Polar angle of direction of scattered light relative to incident direction |
| $\phi$ | Radian | Azimuthal angle of direction of scattered light relative to incident direction |
| $d\Omega$ | Sr | Differential solid angle $\sin\theta d\theta d\phi$ |
| $\delta$ | | Random number with uniform probability between 0 and 1 |
| $T_{two\ stream}$ | | Total transmission (i.e., direct plus diffuse) as calculated by two stream theory with inputs $\bar{\omega}$ and $g$ from Mie theory |
| $T_{Monte\ Carlo}$ | | Total transmission (i.e., direct plus diffuse) as calculated by Monte Carlo methods with inputs $\bar{\omega}$ and $g$ from Mie theory |
| $\beta_{ext}$ | Mm$^{-1}$ | Extinction coefficient of deposited dust |
| $\beta_{sca}$ | Mm$^{-1}$ | Scattering coefficient of deposited dust |
| $\beta_{abs}$ | Mm$^{-1}$ | Absorption coefficient of deposited dust |
| $L$ | mm | Average thickness of deposited dust layer |
| $\gamma$ | | Slope of linear regression ($T_{measured}$ vs. $T_{model}$) |
| $b$ | | Intercept of linear regression ($T_{measured}$ vs. $T_{model}$) |
| $R^2$ | | Correlation coefficient of linear regression |
| $RMSE$ | | Root mean square error |
| $MBE$ | | Mean bias error |
| $T_{model}$ | | Placeholder for either $T_{two\ stream}$ or $T_{Monte\ Carlo}$ |
| $i$ | | Integer number with $i$ = 1,2,3,...,$N$ |
| $N$ | | Total number of transmittance measurements for a dust sample |
| $\tau_i$ | | Placeholder to denote the optical depth $\tau_0$ of a sample $i$ |

#### 2.2.2. Total transmission and direct beam measurement

The direct beam is the part of the incident beam that is neither scattered nor absorbed by the sample, but transmitted. By removing the non-reflective surface from the SIS configuration shown in Fig. 3, the SIS sensor can measure the forward-hemisphere transmission due to forward-hemisphere scattering plus direct beam transmission (i.e., $T_{fwd} + T_{dir}$) as shown in Fig. 4. This measurement of direct plus diffuse (i.e., forward-hemisphere scattering) transmission is henceforth simply referred to as the total transmission $T_{measured}$ given by

$$T_{measured} = T_{fwd} + T_{dir}. \tag{3}$$

From the total transmission measurement, we obtained $T_{dir}$ by subtracting the forward-hemisphere scattering transmission, yielding

$$T_{dir} = T_{measured} - T_{fwd}. \tag{4}$$

#### 2.2.3. Aerosol optical depth retrieval

For the direct beam, light is extinguished due to scattering and absorption by particles deposited onto the glass slide (e.g., Moosmüller et al., 2009). The direct beam transmission $T_{dir}$, defined as the ratio of unaffected power $P$ and incident power $P_0$, quantifies losses due to particle scattering and absorption, and can be written with the Beer-Lambert law as

$$T_{dir} = \frac{P}{P_0} = e^{-\tau_0'}, \tag{5}$$

where $\tau_0'$ is the measured aerosol optical depth (AOD) of the deposited particle layer. Measurement of the direct beam transmission allows us to retrieve the optical depth AOD $\tau_0'$ as

$$\tau_0' = -\ln T_{dir}. \tag{6}$$

However, SIS measurements are susceptible to angular truncations

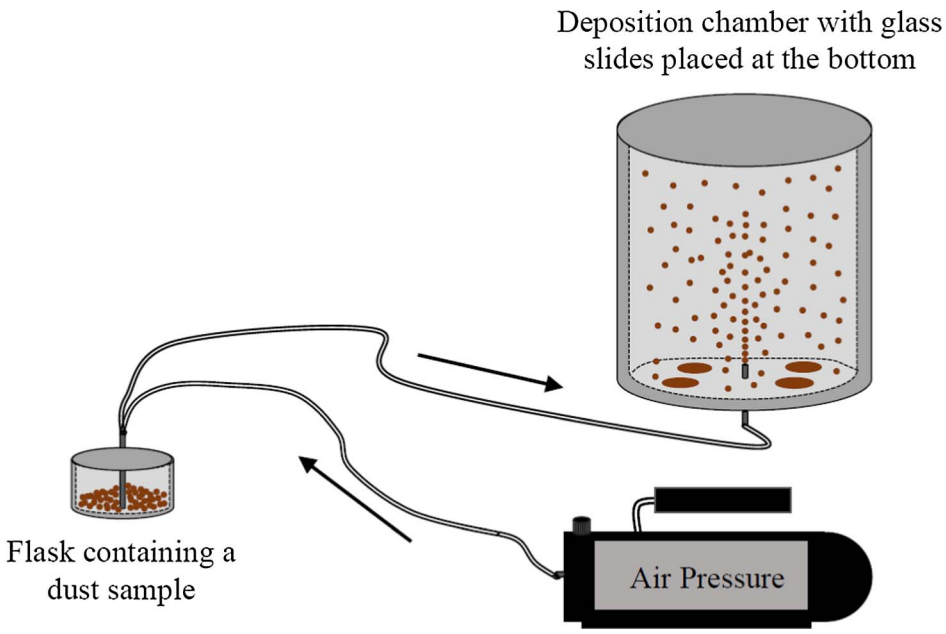


**Fig. 1.** Schematic diagram of mineral dust suspension and deposition experiment. Pressurized air is injected into the sample flask entraining the dust sample and transporting it into the deposition chamber where it gravitationally settles and deposits onto glass slides.

errors due to strongly forward scattering peaks of diffracted light (i.e., a fraction of forward scattering light is eliminated incorrectly, yielding higher measurement of $T_{fwd}$). This has the effect of underestimating the actual AOD $\tau_0$. To correct for this, we used a scaling factor obtained from the delta-Eddington approximation (Liou, 2002)

$$\tau_0 = \frac{\tau_0'}{(1-f\overline{\omega})}, \tag{7}$$

where $\overline{\omega}$ is the single scattering albedo of the dust, and $f$ is the fraction of near-forward scattered and/or diffracted light. This correction factor is explained in more detail in the next section.

### 2.2.4. SIS truncation errors

One consideration of significant importance for the correct distinction between direct and diffuse light is the angular truncation of the SIS detector system. Given that the SIS detector in Fig. 3 uses a non-reflective surface with a finite area to eliminate the power of the direct beam, some near-forward scattered light (mostly diffraction) will inevitably be eliminated incorrectly leading to a lower optical depth retrieval. This is the optical depth detected by the SIS in Eq. (6).

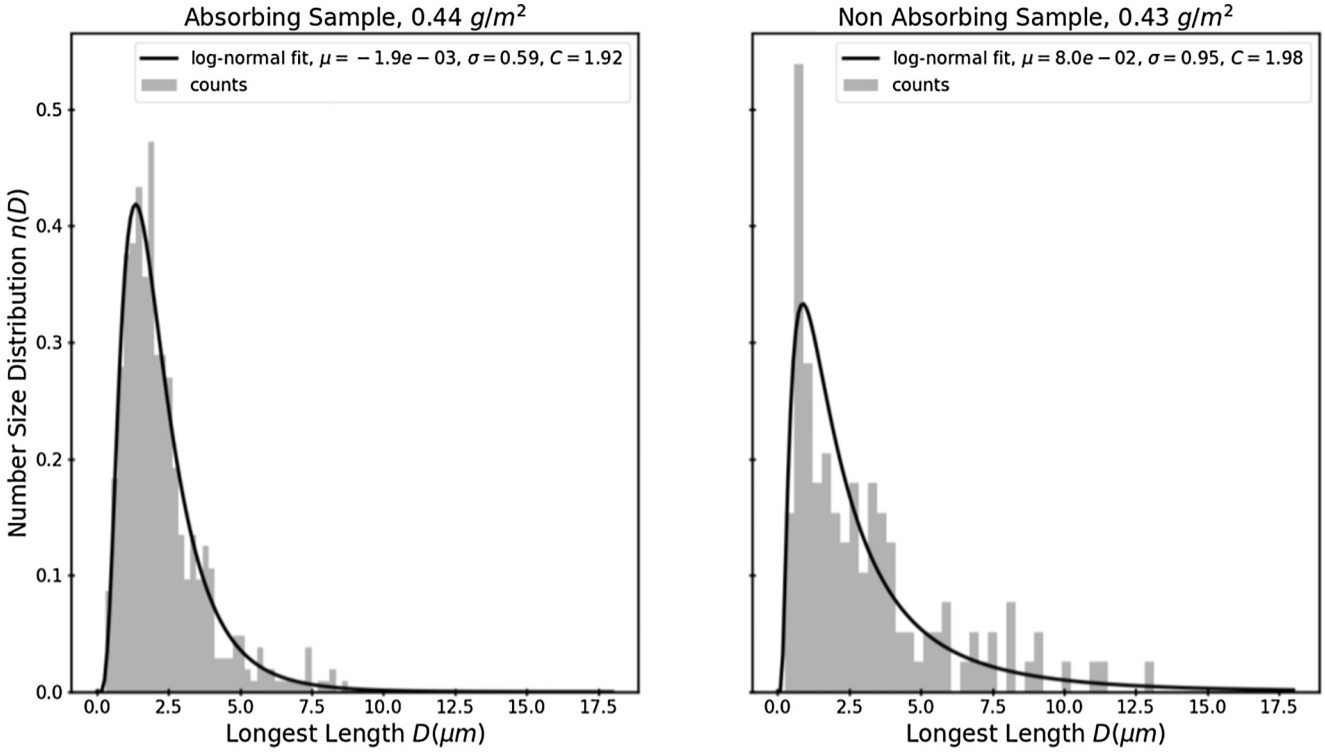


**Fig. 2.** Histogram of longest dimensional length D and log-normal fit for SEM imaging analysis of absorbing dust particles (left) and non-absorbing particles (right).

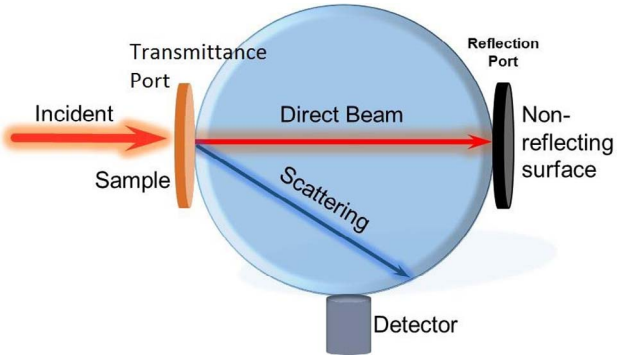


**Fig. 3.** Spherical Integrating Spectrophotometer (SIS) set up for measuring transmission $T_{fwd}$ due to scattering into the forward hemisphere.

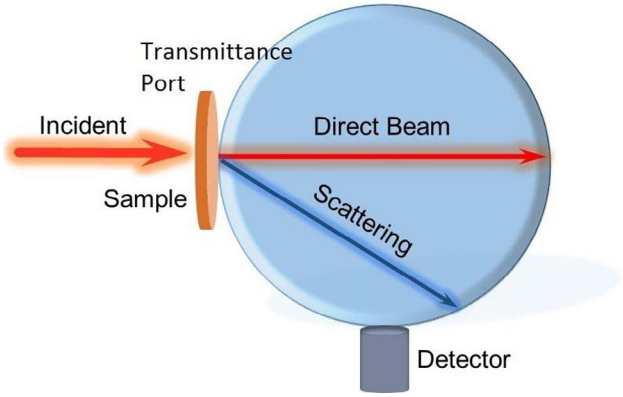


**Fig. 4.** Spherical Integrating Spectrophotometer (SIS) set up for measuring direct beam plus forward scattering transmission.

Truncation errors are accentuated for absorbing particles because diffraction constitutes a larger fraction of the total scattered light (Moosmüller and Arnott, 2003). Correcting this truncation error from the theoretical standpoint is not trivial because it requires very accurate determination of the fraction of diffracted power as a function of optical depth. However, for multiple-scattering, the fraction of diffracted power depends on the optical depth itself, and in general, it is not possible to solve this problem analytically (Liou, 2002). The delta-Eddington approximation (Meador and Weaver, 1980) and its cousin, the delta-M approximation (Wiscombe, 1977) tackle this problem by parameterizing the phase function as a sum of a fractional $f$ Dirac-delta function in the forward direction plus a smooth phase function in all other directions. The phase function of the dust layer medium is expanded as a Legendre polynomial summation (Sobolev, 1975) and this expansion allows us to estimate truncation errors since they are caused by the higher moments of the Legendre expansion. Joseph et al. (1976) showed that the delta-Eddington approximation is a second order Legendre expansion of the phase function in the angular direction. Given that the phase function is not known, we can model a forward peaking phase function using a Henyey-Greenstein phase function (Henyey and Greenstein, 1941). Ultimately, modeling our phase function in this manner estimates the Legendre expansion moment $f \approx g^2$ to second order (e.g., Joseph et al., 1976; Liou, 2002). This factor reveals that our SIS device can distinguish scattered from direct light up to the first moment of the Legendre expansion. However, from the second moment and beyond, some forward scattering peaks are erroneously truncated by the non-reflective surface.

With this estimation of $f$, the $\tau_0'$ detected by the SIS can be used to approximate the actual optical depth $\tau_0$ by substituting $f$ into Eq. (7), yielding

$$\tau_0 = \frac{\tau_0'}{(1-\overline{\omega}g^2)}. \tag{8}$$

Empirically, we found that our theory fits our measurements somewhat better using a correction $f \approx g^{2.3}$ which implies that our detector may be somewhat sensitive to the second moment, and that the truncated near-forward fraction is somewhere between the second and the third moment of the Legendre expansion. However, we do not have any theoretical basis to apply this correction since Legendre polynomial expansions are discreet.

## 3. Theoretical modeling

### 3.1. Multiple scattering: The two-stream approximation

For high particle loading, the assumption of single scattering of light is not applicable since the required single scattering condition of AOD $\tau_0 \ll 1$ is not valid. In this scenario, light interacting with aerosol particles deposited on glass slides or PV modules is likely to undergo multiple scattering events along its optical path through the deposition layer. However, radiative transfer equations are complicated and cannot be solved exactly unless invoking restrictive and unrealistic simplifications. For this reason, there exist a number of radiative transfer models with varying degrees of simplifications and ad hoc applications. The two-stream approximation is a simple model of radiative transfer for parallel layers of a multiple-scattering propagation medium and assumes bi-directionality of light fluxes. The two-stream approximation is derived from assuming homogeneity of the medium as well as azimuthally symmetric phase functions. These simplifications are appropriate for our experiment because a very large number of dust particles are deposited onto a glass slide, constituting a fairly homogeneous medium and because the phase function for these azimuthally randomly oriented particles is expected to be on average azimuthally symmetric, even if the phase function for individual, non-spherical particles is not. Thus, we compare results obtained with the two-stream approximation with our experimental measurements.

To describe the two-stream approximation, let us consider a simplified 1-dimensional system where optical power can only move normal to the plane of the PV module, this simplification can be overcome by extending this method to N-stream theory (Bohren and Clothiaux, 2006). Power moving down (towards the PV module semiconductor) is denoted by $P_\downarrow$, while power moving up by $P_\uparrow$. Neglecting thermal emission (a realistic simplification for dust on PV modules since temperatures are too low for emission within the PV semiconductor spectral response), the two-stream equations of radiative transfer are given by (e.g., Petty, 2006)

$$\frac{d}{d\tau}(P_\downarrow - P_\uparrow) = -(1-\overline{\omega})(P_\downarrow + P_\uparrow), \tag{9}$$

and

$$\frac{d}{d\tau}(P_\downarrow + P_\uparrow) = -(1-\overline{\omega}g)(P_\downarrow - P_\uparrow), \tag{10}$$

where $\overline{\omega}$ is the SSA defined as the ratio of single-scattering and extinction cross-section $\left(\frac{\sigma_{sca}}{\sigma_{ext}}\right)$ and $g$ is the asymmetry parameter (Andrews et al., 2006); these are also the key aerosol optics intensive parameters used for atmospheric aerosol radiative forcing calculations (Chylek and Wong, 1995; Hassan et al., 2015; Moosmüller and Ogren, 2017). The boundary conditions for our two-stream model at $\tau = 0$ and at $\tau = \tau_0$ (where $\tau_0$ is the AOD of the dust layer) are given in Fig. 5 with $R$ being the total reflectance (i.e., backward hemispheric reflection), while $T$ is the total transmittance through the dust layer accounting for both directly (i.e., unaffected) and diffusely (i.e., single or multiple scattered) transmitted radiation.

When the system of coupled differential equations (9) and (10) is solved using the boundary conditions specified in Fig. 5, the total

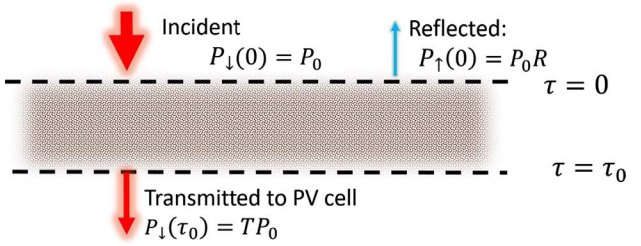


**Fig. 5.** Two-Stream approximation reference system and boundary conditions. $P_0$ is the incident power, R is the total reflectance, T is the total transmittance.

transmission $T$ at optical depth $\tau_0$ can be expressed as (Liou, 2002)

$$T(\tau_0,\overline{\omega},g) = \frac{2}{2\cosh(K\tau_0) + \frac{\sinh(K\tau_0)}{K}[2-\overline{\omega}(1+g)]}, \tag{11}$$

where $K \equiv \sqrt{(1-\overline{\omega})(1-\overline{\omega}g)}$. This equation is a very simple analytical solution for the total transmission $T$ into the forward direction through a layer of scattering and absorbing medium. The transmission equations give the total (i.e., diffuse plus direct) transmission $T$ as a function of two intensive particle properties, SSA $\overline{\omega}$ and asymmetry parameter $g$, as well as one extensive property of the particle layer, its optical depth $\tau_0$. Typical values of $\overline{\omega}$ for dust commonly range from $\sim 0.4$ to $\sim 1$ (Engelbrecht et al., 2016), while $g$ commonly ranges from $\sim 0.45$ to $\sim 0.65$ (Fiebig and Ogren, 2006).

#### 3.1.1. Intensive parameter of optical efficiency loss: Asymmetry parameter $g$

The asymmetry parameter for single scattering by particles is given by (e.g., Andrews et al., 2006; Videen et al., 1998)

$$g = \frac{\int_{4\pi} \frac{d\sigma_{sca}}{d\Omega}\cos\theta d\Omega}{\int_{4\pi} \frac{d\sigma_{sca}}{d\Omega} d\Omega}, \tag{12}$$

where $\frac{d\sigma_{sca}}{d\Omega}$ is the angular distribution of scattered power. In spherical coordinates, $\theta$ is the polar angle, $\phi$ is the azimuthal angle, and $d\Omega = \sin\theta d\theta d\phi$ is the differential solid angle. From Eq. (12), it follows that $g$ is the mean cosine of the angular scattering power distribution. One-dimensionally, $\frac{1-g}{2}$ can be interpreted as the probability that scattered light will change its direction from up to down or vice versa, while $\frac{1+g}{2}$ is the probability that scattered light will continue in its original direction after scattering (Bohren, 1987). If the size distribution of particles is not monodisperse, the angular distribution $\frac{d\sigma_{sca}}{d\Omega}$ must be integrated with respect to the particle size number distribution $n(D)$ (i.e., the number of particles with diameter $D$). In either case, $\frac{d\sigma_{sca}}{d\Omega}$ can be calculated using light scattering theory, such as Mie theory (Mie, 1908), T-matrix (e.g., Liu et al., 2008; Mishchenko et al., 2007), or discrete dipole approximation (Yurkin and Hoekstra, 2011). A simple model is Mie theory, an exact solution for homogeneous, spherical particles where $\frac{d\sigma_{sca}}{d\Omega}$ is only dependent on the particles' complex refractive index $m$ and diameter $D$ and the wavelength $\lambda$ of the incident radiation. In the multiple-scattering regime, the optical averaging of a multitude of particles allows us to approximate the overall phase function of all particles as that of a collection of spheres. However, our choice of scattering theory can be improved for accuracy. It is important to note that dust particles are generally not homogeneous spheres but rather irregularly shaped and inhomogeneous. In our current application, the term diameter is used to describe the longest dimensional length of a particle deposited on our glass slide (i.e., the diameter of an enclosing sphere). Non-spherical particles usually differ in scattering cross section and asymmetry parameter from spherical particles though not more than by 10% (Mishchenko et al., 1997). Improvements in scattering theory can also include the effect of the glass substrate, which has been discussed by Videen and Ngo (1997) and by Mackowski (2010). These scattering theories can be used to model azimuthally symmetric particles. For irregular particles such as dust, the only available particle-on-substrate light scattering solution is that of discrete dipole approximation with substrate interaction (e.g., Yurkin and Huntemann, 2015) although these calculations can be computationally very time consuming.

In our case, the angular distribution of scattered power, integrated over a polydisperse size distribution can be written as

$$\frac{d\sigma_{sca}(m,\lambda)}{d\Omega} = \int_{D_1=0}^{D_2=\infty} \frac{d\sigma_{sca}(D,m,\lambda)}{d\Omega} n(D) dD, \tag{13}$$

where we integrate over the size dependence of the differential scattering cross section weighed by the number size distribution $n(D)$. In practice, the integration of Eq. (13) is done numerically, and the limit $D_2$ is chosen such that the scattering from particles with $D > D_2$ approaches zero. It is necessary to use a nearly continuous function $n(D)$ so that accumulation of errors by numerical integration is minimal. Hence, prior to integration, $n(D)$ should be fitted by a continuous function, typically a log-normal size distribution function (e.g., Piedra, 2014) such as that of Eq. (1).

#### 3.1.2. Intensive parameter of optical efficiency loss: Single scattering albedo (SSA) $\omega$

For a single particle, the optical power removed from the direct beam by scattering from a particle is proportional to $\sigma_{sca}$, while the optical power absorbed and converted into heat is proportional to the absorption cross section $\sigma_{abs}$. The extinction cross section $\sigma_{ext} = \sigma_{abs} + \sigma_{sca}$ is the sum of absorption and scattering cross section. The SSA $\overline{\omega}$ is an intensive optical property of a particle that indicates the fraction of light extinction due to scattering. SSA is defined as

$$\overline{\omega} = \frac{\sigma_{sca}}{\sigma_{ext}}. \tag{14}$$

Just like the asymmetry parameter $g$, the SSA $\overline{\omega}$ is an intensive particle property, independent of the number of particles involved. For homogeneous, spherical particles, scattering, absorption, and extinction cross sections and consequently SSA $\overline{\omega}$can be calculated with Mie theory and depend exclusively on the particle complex refractive index $m(\lambda)$, diameter $D$, and the wavelength $\lambda$ of the incident radiation. If the size distribution of particles is not monodisperse, an integration over the size distribution similar to Eq. (13) is needed. Here, we have used a Mie calculation routine initially developed in Fortran by Bohren and Huffman (1983) and translated into Python by Kaiser (2012).

### 3.2. Monte Carlo method

Monte Carlo methods (Metropolis and Ulam, 1949) are appealing given the relative simplicity of their implementation and the increasing power of modern computers. For optical propagation calculations, these methods model the optical path of many photons, and keep track of each photon's fate. The implementation used here closely follows the logical flow of Prahl et al. (1989) with the difference that our implementation is one-dimensional (1-D) and uses a dimensionless optical depth (i.e., it does not require the actual physical thickness of the dust layer).

The logical flow of our code can be seen in Fig. 6. We start by generating a photon in the down direction, which has a probability $\delta$ of propagating directly through the deposited dust layer

$$\tau = -\ln\delta, \tag{15}$$

where $\delta$ is a number randomly generated with equal probability to be between 0 and 1. If the generated photon propagates beyond $\tau > \tau_0$, it is counted as transmitted. Otherwise, the photon is inside the dust layer medium and is either scattered or absorbed. To decide if the photon is absorbed or scattered, we generate another $\delta$ and allow the photon to be absorbed if $\delta > \overline{\omega}$, or scattered if $\delta > \overline{\omega}$.

If the photon is scattered, the photon's direction will change. To

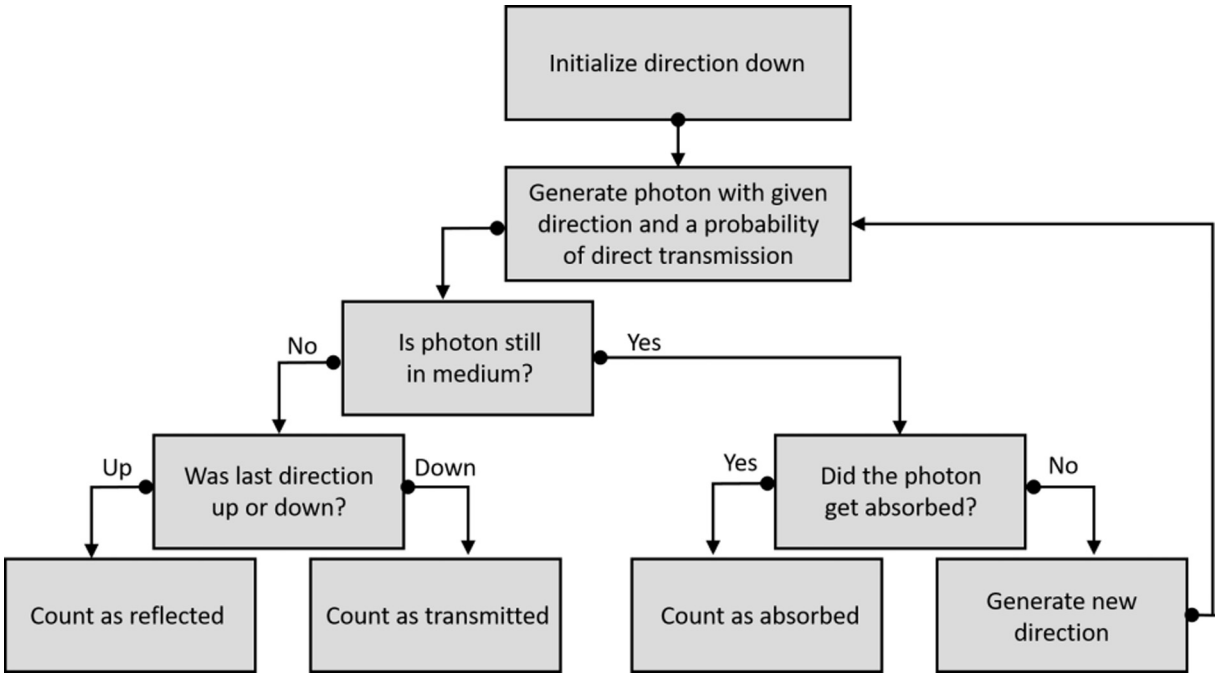


**Fig. 6.** Logical flow of the Monte Carlo method used here.

model this directional change consistently with two-stream theory, we generate another $\delta$ at random, and turn the photon into the opposite direction if $\delta > \frac{1+g}{2}$ (Ch. 5, Bohren and Clothiaux, 2006), or else keep its original direction if $\delta < \frac{(1+g)}{2}$. It is noteworthy that expansion of this method to 3-D geometry is straightforward as it requires only simple vector rotations of the propagating photon direction along appropriate planes of scattering. These rotations can be implemented with quaternions, Euler angles, or the Rodriguez formula.

## 4. Results and discussion

Our objective is to understand optical losses of PV modules due to deposition of particles and to develop simple models that can be used to estimate such optical losses. The models used here are directly applicable only for direct sunlight (i.e., black sky) and for normal incidence, and assume that no diffuse radiation exists above the deposited dust layer. However, diffuse radiation (incoming radiation scattered by atmospheric gases and particles, including clouds) contributes to the total solar radiation received by PV module. Depending on the solar zenith angle, wavelength, and atmospheric conditions, the fraction of diffuse radiation in total solar radiation can range from ~0% for clear days and near-infrared radiation to ~100% on cloudy days (Kaskaoutis and Kambezidis, 2009); future work should expand directionality simplifications and incorporate the attenuation of diffuse radiation for instance by using ray-tracing techniques (Zorrilla-Casanova et al., 2013), or by expanding incident directions using the Monte Carlo method used here.

### 4.1. Experimental results

Figs. 7 and 8 show an overview of our experimental measurements of total transmission as a function of dust mass deposited per unit area (i.e., mass density) for the spectral range of 400 to 1400 nm and for absorbing and non-absorbing dust, respectively. For comparison with previous work, Fig. 9 shows our measurements at wavelength $\lambda = 600$ nm together with results compiled by Xu et al. (2017). Our measurements for the non-absorbing sample agree well with the results of Xu et al. (2017), indicating that the dust deposited in their study was mostly non-absorbing as expected for most dust sources (Engelbrecht et al., 2016). In Fig. 9, we also show measurements compiled by Hegazy (2001) in a study of the decrease in transmission of PV modules as a function of deposited dust mass density for different tilt angles of PV modules. Hegazy (2001) made these measurements in Minia, Egypt, and they agree better with our measurements for absorbing dust, suggesting that in this region deposition is dominated by absorbing dust. In addition, the 3-D surface plots of Figs. 7 and 8 show a clear distinction between transmission of the absorbing and the non-absorbing dust. For instance, notice that for the absorbing dust sample at a deposition mass density of 10 g/m$^2$, the minimum transmission occurs near a wavelength of 550 nm with a forward hemispheric transmission of ~0.3. In contrast, for the non-absorbing dust sample, at 10 g/m$^2$, the minimum forward hemispheric transmission is ~0.6. In this simple example, assuming PV module efficiency is proportional to optical transmission, the efficiency of the PV module at 550 nm covered by 10 g/m$^2$ of non-absorbing dust would be about twice that of a PV module covered by 10 g/m$^2$ of absorbing dust. This comparison highlights the importance of optical characterization of dust for PV module power forecasting and location selection. While deposition of absorbing dust could be highly detrimental for PV module efficiency, transmission losses caused by non-absorbing particles would be significantly smaller for the same deposition mass density.

Another important observation is that transmission losses are not limited to the spectral region of very high imaginary refractive index of the dust type. Indeed, SSA is the lowest for intermediate values of imaginary refractive index, but higher for both very low and very high values (Moosmüller and Sorensen, 2018). We also observe that our measurements of total transmission vary strongly as a function of deposited mass density but not as much as a function of wavelength. Such near constancy of total transmission through the spectrum highlights the dependency of optical transmission on the different particle sizes that a sample of dust could have. Even though a single particle's SSA can change substantially as a function of wavelength depending on its size and imaginary refractive index, the overall SSA for the whole dust sample remains fairly constant through the spectrum. This result is reasonable since losses into the forward hemisphere due to absorption and scattering are governed by the ratio of particle diameter to particle skin depth as opposed to the imaginary refractive index alone (Piedra and Moosmüller, 2017; Wang et al., 2015).

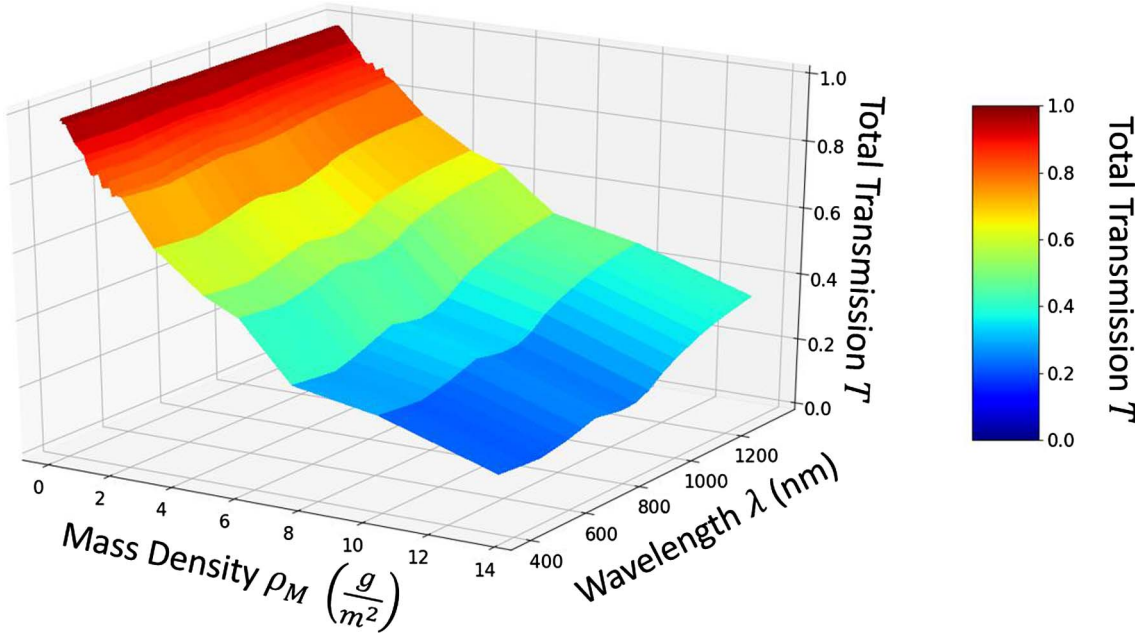


**Fig. 7.** Absorbing dust sample total transmission $T$ as a function of mass density and wavelength. For clarity, $T$ is plotted both as surface and as color-scale.

### 4.2. Theoretical results and their comparison with experimental results

For our absorbing hematite powder sample and non-absorbing dust sample, Fig. 10 displays a comparison of measurements and calculations of total transmission $T$ as a function of deposited particle AOD $\tau_0$ at wavelength $\lambda$ = 410, 600, and 780 nm. The left and right columns contain measurements and calculations for the absorbing and the non-absorbing dust sample, respectively. We use the $T_{measured}$ to denote SIS measurements of total transmission, $T_{two\ stream}$ to denote total transmission $T$ calculated with Eq. (11), and $T_{Monte\ Carlo}$ for $T$ calculated with the Monte Carlo method. The particle number size distribution $n(D)$ used was obtained by log-normal fit to an experimental particle number size distribution acquired from microscopy images of the deposited sample (see Section 2.1). The quantities $\varpi$ and $g$ were calculated using Mie theory as discussed in Section 3.1.1 and Section 3.1.2, respectively. The refractive indices for the absorbing hematite sample were given by Querry (1985). The non-absorbing sample had not been characterized by refractive index but by SSA $\varpi$ by Engelbrecht et al. (2016). As with the absorbing sample, we have measured $n(D)$ by microscope image analysis and estimated its real part of the refractive index to be $m_r \sim 1.5$. The measured $\varpi$ and the assumed $m_r$ allowed us to retrieve the imaginary part of the refractive index $m_i$, which yields the asymmetry parameter by applying Eq. (12) with Mie theory, under the assumption of homogeneous spherical particles. In Table 3, we give a summary of values of SSA $\varpi$, asymmetry parameter $g$, and refractive index $m$ used to obtain the curves shown in Fig. 10.

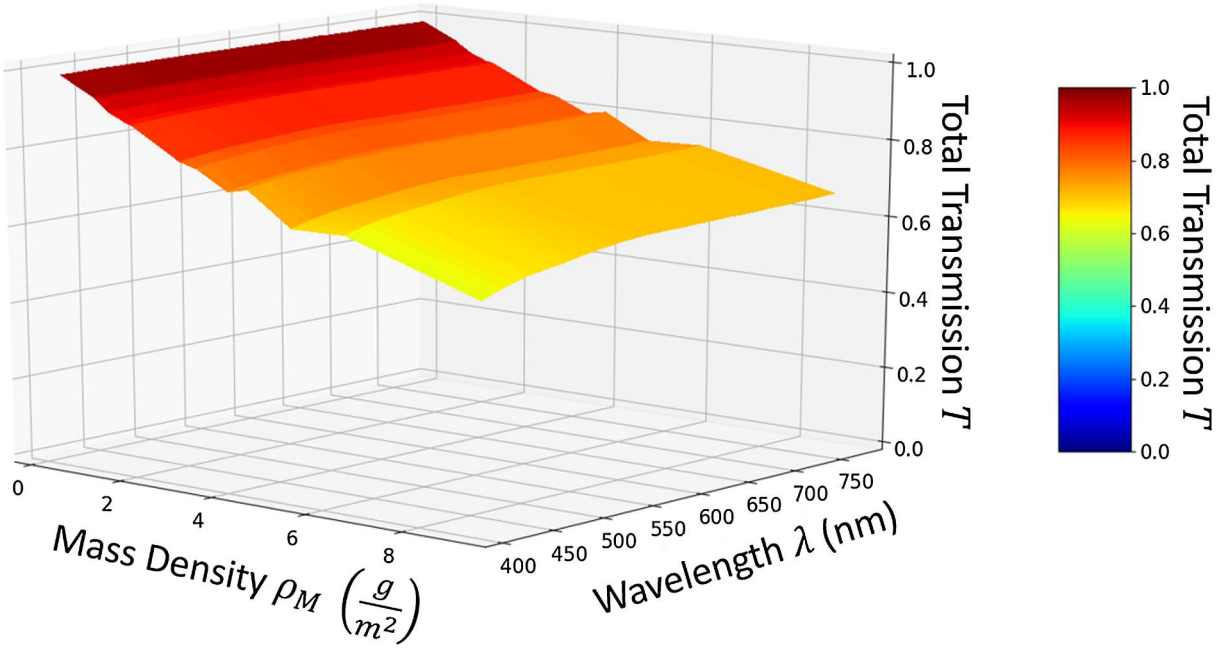


**Fig. 8.** Same as Fig. 7 but for non-absorbing dust sample.

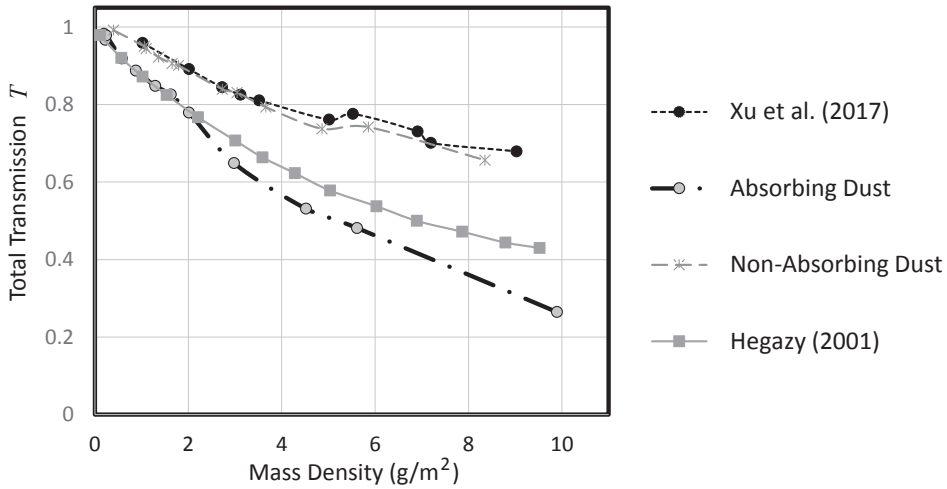


**Fig. 9.** Total transmission as a function of deposited dust mass density measured at $\lambda = 600$ nm by our SIS. We also show 1 minus the decrease of transmission of PV modules compiled by Xu et al. (2017) and Hegazy (2001).

### 4.3. Evaluation of methods

We now move our attention to quantitatively characterizing the agreement of our theoretical calculations with our experimental measurements results as shown in Fig. 7. We evaluate agreement by plotting our theoretical values as a function of our measured ones. For both pairs of datasets, that is ($T_{measured}$, $T_{two\ stream}$) and ($T_{measured}$, $T_{Monte\ Carlo}$), a linear regression was performed, yielding slope $\gamma$, intercept $b$, and correlation coefficient $R^2$. Perfect agreement would mean that $\gamma = 1$, $b = 0$, and $R^2 = 1$. Fig. 11 displays a comparison of total transmission obtained by models plotted as a function of total transmission obtained by measurement for the same wavelengths used to calculate Fig. 10

**Table 3**
Summary of input values for curves displayed in Fig. 10.

| | Absorbing sample | | | Non-absorbing sample | | |
|---|---|---|---|---|---|---|
| $\lambda$ (nm) | $\varpi$ | $g$ | $m$ | $\varpi$ | $g$ | $m$ |
| 410 | 0.630 | 0.778 | $2.72 + i1.2$ | 0.983 | 0.802 | $1.5 + i3.3 \times 10^{-4}$ |
| 600 | 0.612 | 0.784 | $3.14 + i0.16$ | 0.997 | 0.780 | $1.5 + i8.5 \times 10^{-5}$ |
| 780 | 0.649 | 0.743 | $2.78 + i0.032$ | 0.999 | 0.768 | $1.5 + i3.7 \times 10^{-5}$ |

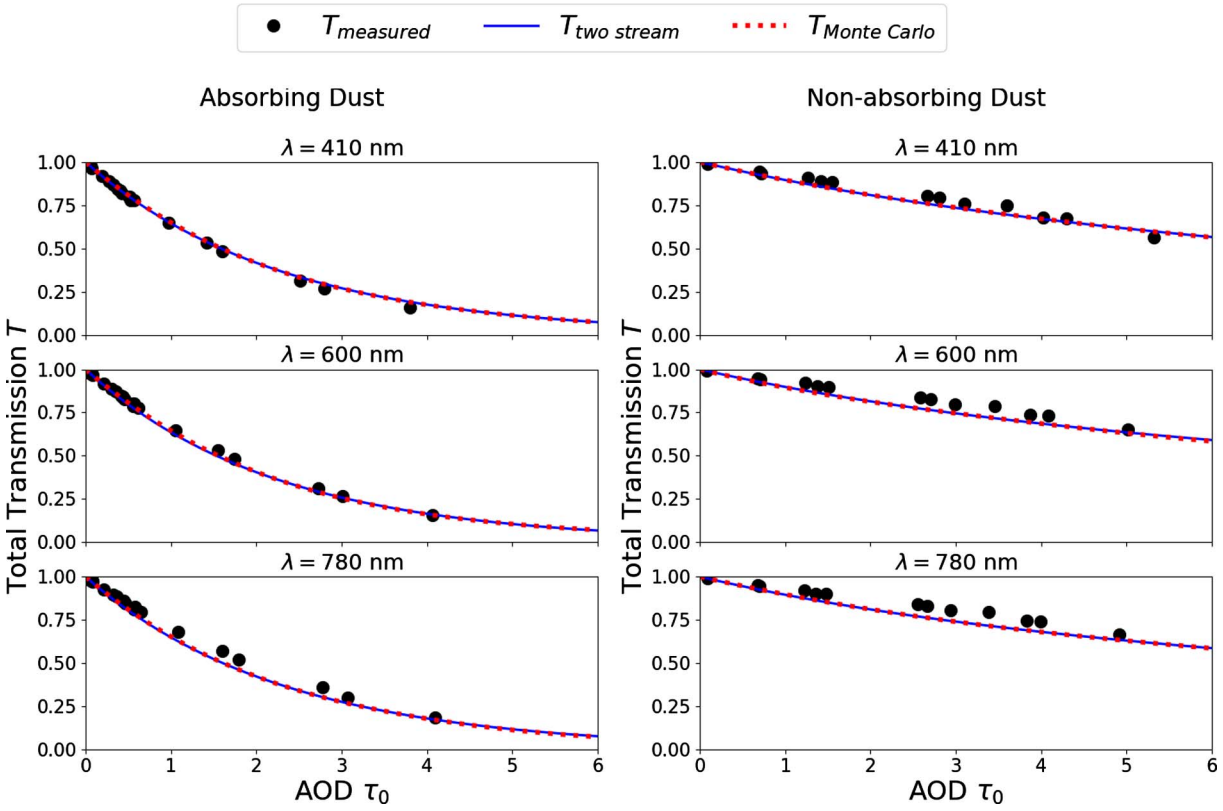


**Fig. 10.** Total transmission T as a function of AOD $\tau_0$ at wavelengths $\lambda = 410$,600, and 780 nm from measurements ($T_{measured}$, round dots), against two-stream theory ($T_{two\ stream}$, solid lines) and Monte Carlo technique ($T_{Monte\ Carlo}$, dotted lines) for absorbing (left column) and non-absorbing (right column) dust deposited onto glass slides. Input parameters for two-stream and Monte Carlo calculations are shown in Table 3.

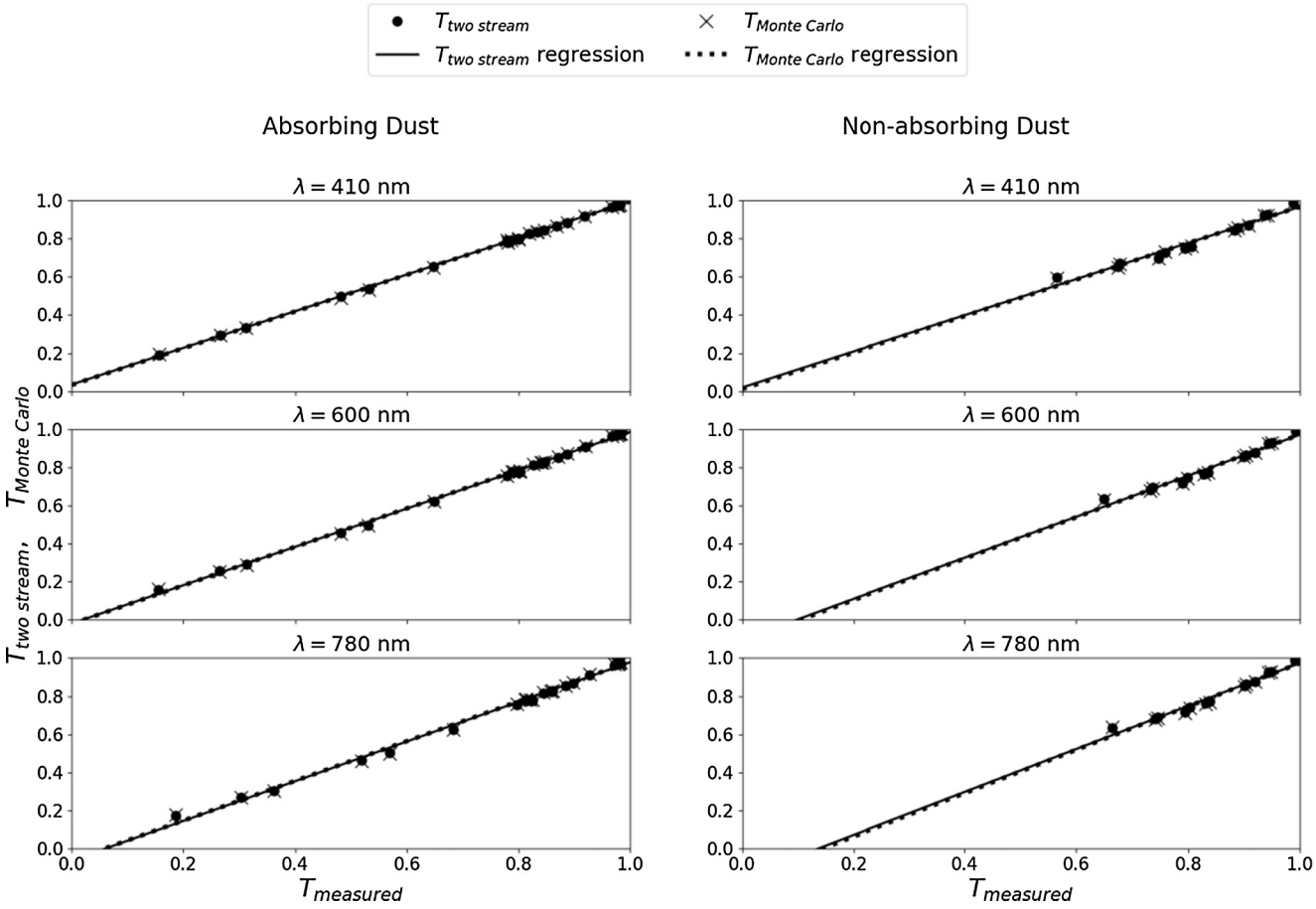


**Fig. 11.** Model total transmission as a function of measured one. Perfect agreement would be reached if slope $\gamma = 1$, intercept $b = 0$, and correlation coefficient $R^2 = 1$.

($\lambda$ = 410, 600, and 780 nm). In addition, we calculate the root mean square error *RMSE* defined as

$$RMSE = \sqrt{\frac{1}{N}\sum_{i=1}^{N}\left[\frac{T_{model}(\varpi,g,\tau_i) - T_{measured}(\tau_i)}{T_{measured}(\tau_i)}\right]^2}, \quad (16)$$

as well as the mean bias error *MBE* defined by

$$MBE = \frac{1}{N}\sum_{i=1}^{N}\frac{T_{model}(\varpi,g,\tau_i) - T_{measured}(\tau_i)}{T_{measured}(\tau_i)}, \quad (17)$$

where $N$ is the total number of measurements and $i = 1,2,...,N$. Each total transmission measurement has been done at a different optical depth $\tau_0 = \tau_i$, and we are comparing with either two-stream theory, or Monte-Carlo method as calculated with the inputs $\varpi$ and $g$ listed in Table 3. The subscript "*model*" stands for either "*two stream*" or "*Monte Carlo*".

Tables 4 and 5 summarizes the evaluation metrics: slope, intercept, correlation coefficients obtained from linear regression as well as *RMSE* and *MBE* for the absorbing sample, while Tables 6 and 7 do the same

**Table 4**
Slopes γ, y-intercepts b, correlation coefficients $R^2$, root mean square error (RMSE) and mean bias error (MBE) obtained from linear regressions in Fig. 10 for evaluation of two-stream theory with the absorbing sample.

| Absorbing sample: Two-stream theory | | | | | |
|---|---|---|---|---|---|
| λ (nm) | γ | b | $R^2$ | *RMSE* | *MBE* |
| 410 | 0.962 ± 0.004 | 0.034 ± 0.003 | 1.00 | 0.0669 | −0.0047 |
| 600 | 1.006 ± 0.009 | −0.019 ± 0.007 | 0.99 | 0.0673 | −0.0048 |
| 780 | 1.042 ± 0.016 | −0.063 ± 0.013 | 0.99 | 0.0668 | −0.0047 |

**Table 5**
Same as Table 4 for evaluation of Monte-Carlo method with the absorbing sample.

| Absorbing sample: Monte-Carlo method | | | | | |
|---|---|---|---|---|---|
| λ (nm) | γ | b | $R^2$ | *RMSE* | *MBE* |
| 410 | 0.969 ± 0.004 | 0.034 ± 0.003 | 1.00 | 0.0668 | −0.0047 |
| 600 | 1.013 ± 0.006 | −0.019 ± 0.005 | 0.99 | 0.0672 | −0.0048 |
| 780 | 1.048 ± 0.017 | −0.068 ± 0.014 | 0.99 | 0.0667 | −0.0047 |

**Table 6**
Same as Table 4 for evaluation of two-stream theory with the non-absorbing sample.

| Non-absorbing sample: Two-stream theory | | | | | |
|---|---|---|---|---|---|
| λ (nm) | γ | b | $R^2$ | *RMSE* | *MBE* |
| 410 | 0.948 ± 0.060 | 0.019 ± 0.049 | 0.98 | 0.0242 | −0.0017 |
| 600 | 1.076 ± 0.066 | −0.105 ± 0.056 | 0.98 | 0.0236 | −0.0017 |
| 780 | 1.127 ± 0.063 | −0.154 ± 0.056 | 0.98 | 0.0241 | −0.0017 |

**Table 7**
Same as Table 4 for evaluation of Monte-Carlo method with the non-absorbing sample.

| Non-absorbing sample: Monte-Carlo method | | | | | |
|---|---|---|---|---|---|
| λ (nm) | γ | b | $R^2$ | *RMSE* | *MBE* |
| 410 | 0.954 ± 0.057 | 0.015 ± 0.047 | 0.98 | 0.0241 | −0.0017 |
| 600 | 1.081 ± 0.063 | −0.107 ± 0.054 | 0.99 | 0.0232 | −0.0016 |
| 780 | 1.120 ± 0.070 | −0.147 ± 0.060 | 0.98 | 0.0239 | −0.0017 |

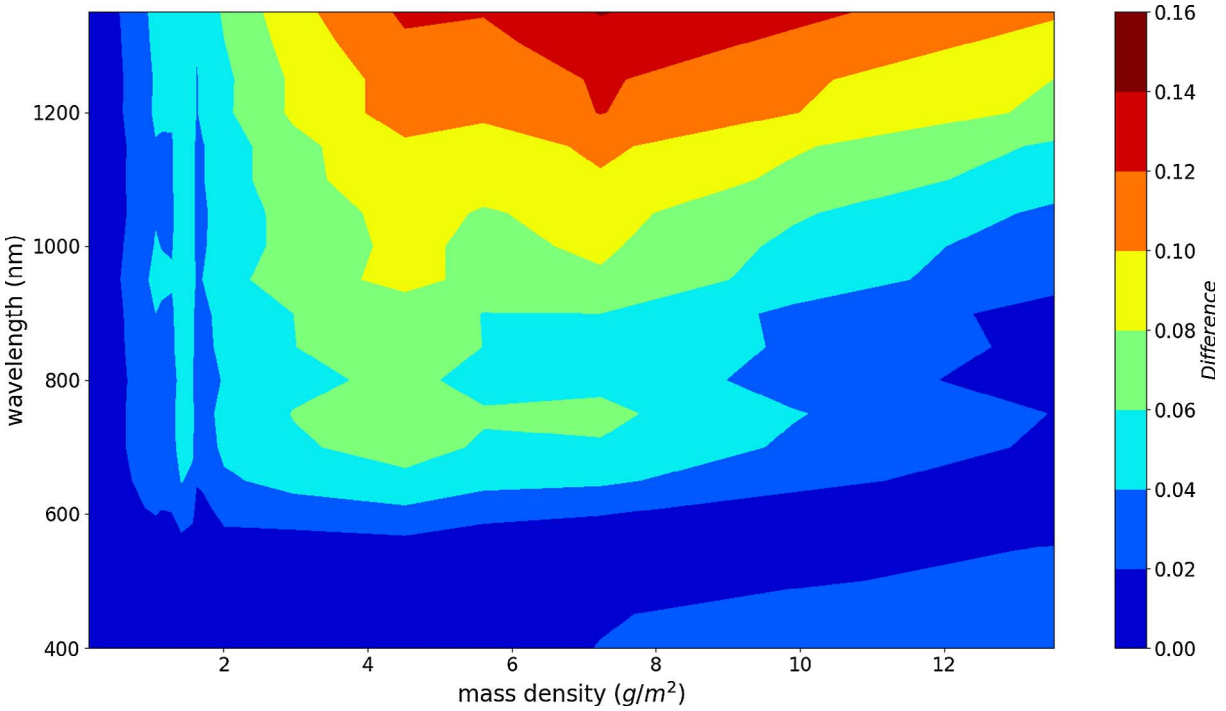


**Fig. 12.** Difference between measurement and two-stream calculation of transmission for absorbing dust as a function of wavelength and deposition mass density.

for the non-absorbing sample.

In general, we see that both methods, two-stream and Monte Carlo, yield very similar transmissions, including nearly identical slopes, intercepts, and correlation coefficients when compared by linear regression with our experimental results. All evaluation metrics between two-stream theory and Monte Carlo methods are nearly identical. The linear regression for the absorbing sample has an intercept closer to zero than for the non-absorbing sample. The linear regression intercepts for both absorbing and non-absorbing samples become negative as wavelength increases. Overall, linear regressions between two-stream and Monte Carlo transmissions and experimental transmissions have slopes close to one, and intercepts close to 0 which indicates good agreement between theory and experiment. In addition, the correlation coefficients are very close to one, indicating that these methods are very good at predicting the total transmission as a function of optical depth for absorbing and non-absorbing mineral dust deposits. In addition, the *RMSE* and *MBE* for both absorbing and non-absorbing samples are very small, indicating an overall good agreement between our models and measurements. In our comparisons, the absorbing sample has larger *RMSE* and *MBE* than the non-absorbing counterpart.

Figs. 12 and 13 illustrate the absolute difference between our experimental measurements and theoretical calculations of total transmission $T$ for the absorbing and non-absorbing samples, respectively. This difference is defined as

$$Difference = |T_{measured} - T_{calculated}|, \tag{18}$$

and is plotted as a color-scale contour. Comparisons with Monte Carlo results are obviated since these results differ from those of two-stream theory by less than 1%. In the case of absorbing dust (Fig. 12), two-stream method transmission results remain within $\lesssim 0.1$ of the experimental results for almost the entirety of the $\rho_m$ -$\lambda$ domain, reaching $0.1 \lesssim Difference \lesssim 0.16$ at large wavelengths $\lambda \gtrsim 1100$ nm and high mass density $\rho_m \gtrsim 6$ g/m$^2$.

A comparison of two-stream model calculations and measurements of transmission for non-absorbing dust (Fig. 13) shows good agreement for the spectral range of 410 to 780 nm (this sample had not been characterized beyond this spectral range), with differences in transmission less than 0.08. These results suggest that two-stream theory and Monte Carlo methods can estimate PV module transmission decrease for most practical purposes for absorbing dust and non-absorbing dust.

## 5. Additional work needed for forecasting applications

This work compares transmission of monochromatic light into a dust-deposited PV module, predicted by two radiative transfer models with experimental results. Additional work is needed for PV module efficiency forecasting. The flow chart in Fig. 14 describes the problem space of solar efficiency forecasting and the role of this work in its solution. Two models need to be merged: deposition models and optical models. Deposition models are needed to forecast the dust mass density $\rho_m$ deposited onto the PV module (e.g., Javed et al., 2017; Said and Walwil, 2014). Data-intensive, location-specific deposition models (e.g., deep neural networks) are likely to yield accurate predictions of dust accumulation. If the volume density $\rho$ (i.e., mass per unit volume) of the deposited dust is known, the ratio $\frac{\rho_m}{\rho} = L$ estimates the average thickness $L$ of the dust layer. Furthermore, optical models are needed to relate deposited dust mass density to the extinction coefficient $\beta_{ext}$ (i.e., fraction of light extinguished per unit optical path length) and subsequently the optical depth $\tau_0 = \beta_{ext} L$. Furthermore, optical characterization is needed to obtain the dust's scattering coefficient $\beta_{sca}$ and the absorption coefficient $\beta_{abs}$; the combination of two of these coefficients yields the needed single scattering albedo $\varpi = \frac{\beta_{sca}}{\beta_{ext}} = \frac{\beta_{ext} - \beta_{abs}}{\beta_{ext}}$. The radiative transfer models used here also depend on the asymmetry parameter $g$. However, dust particles are highly scattering in the forward direction and Eq. (11) is largely dominated by changes of $\varpi$ rather than of $g$. Hence, a typical value (e.g., $g \sim 0.75$) can be assumed. The radiative transfer models used here do not include different incident angles of solar irradiance. This can be done by simply modifying the optical path along the dust sample with respect to the incidence angle. In the same manner, a diffuse irradiance component should be integrated with respect to all incident angles. An appropriate treatment of inhomogeneous and non-spherical dust particles may also be needed to yield correct $\varpi$ and $\tau_0$ for such dust types. Finally, the transmission response needs to be weighted with respect to solar spectrum and spectral response of the PV module.

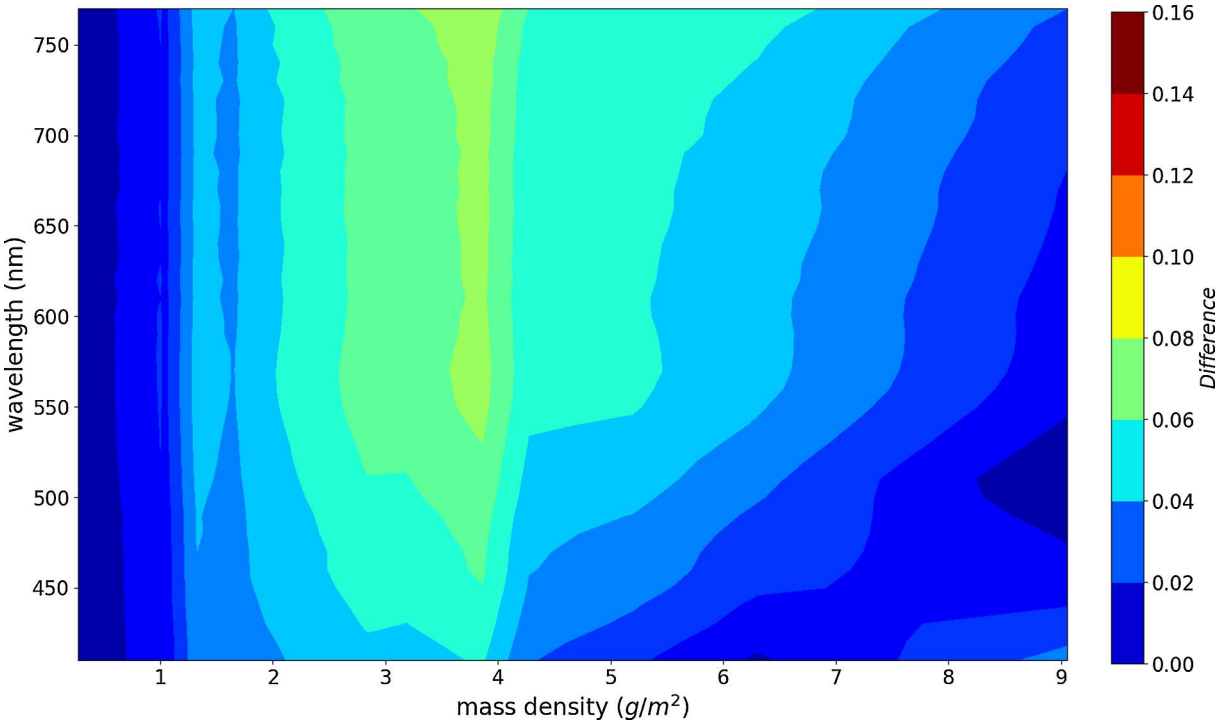


**Fig. 13.** Difference between measurement and two-stream calculation of transmission for non-absorbing dust as a function of wavelength and deposition mass density.

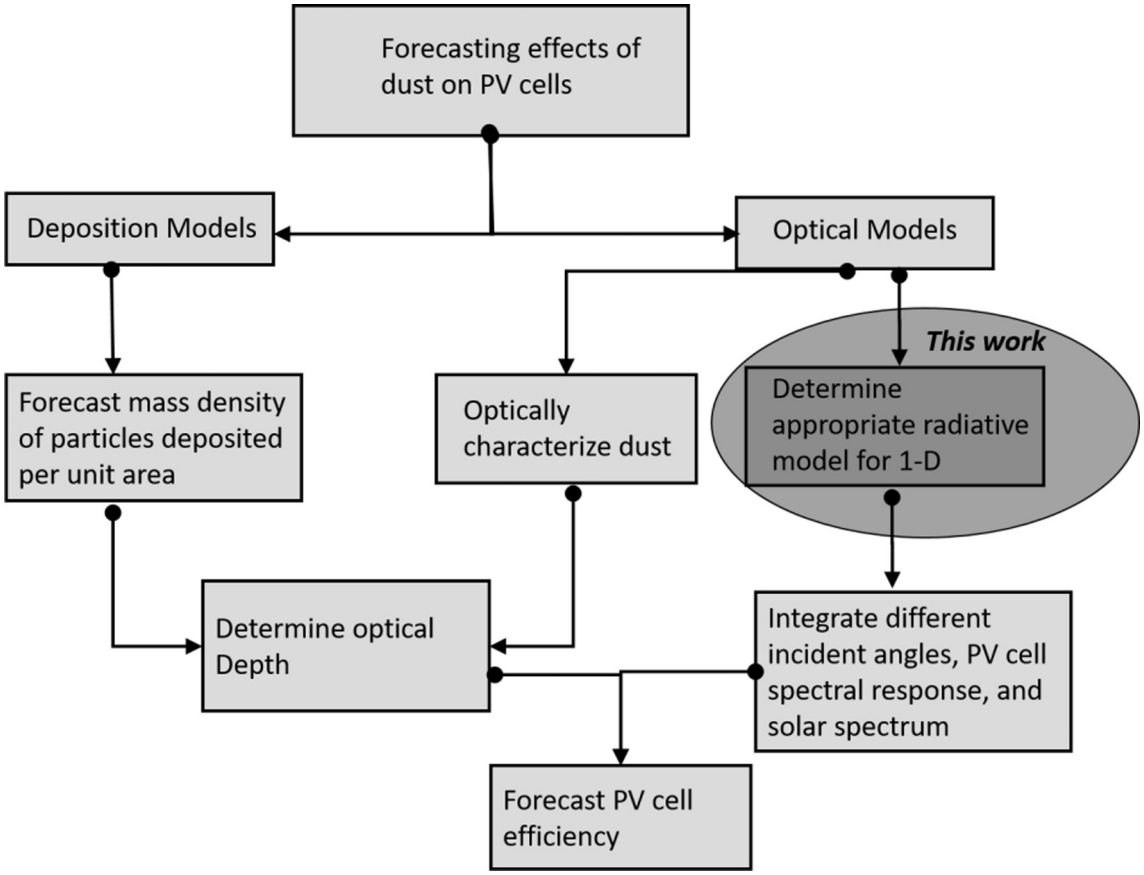


**Fig. 14.** Description of how optical models and deposition models can be combined to contribute to PV module optical efficiency forecasting. The oval represents the work discussed here.

It is important to note that in the context of this paper, the term "PV module efficiency forecasting" refers only to power losses due to decreased irradiance entering the PV module semiconductor due to dust deposition. However, PV module power generation is also affected by non-optical effects such as PV module temperature, voltage dependence on temperature, and electrical mismatches between PV modules. Some of these non-optical effects can be influenced by particles deposition on PV modules, and they affect the overall electric power generation of a PV module. Non-optical factors are very important, in addition to the optics of dust deposition considered here, when forecasting the overall power generation of PV modules.

## 6. Conclusion

This paper examines the spectral transmission of radiation through dust covered glass slides as surrogate for dust covered PV modules. A major conclusion is the strong variation of total transmission as a function of the single scattering albedo (SSA) of the dust. Our experimental results indicate that forward hemispheric transmission decreases approximately linearly with deposited mass per unit area $\rho_m$. However, the slope of this decrease is highly sensitive to the absorptivity of the dust. This nearly linear relationship between total transmission and deposited dust mass density is a result of low optical depth in our experiments (i.e., $\tau_0 < 7$), and a hyperbolic relationship similar to Eq. (11) is expected for larger mass loadings. Furthermore, our experimental and theoretical results for the total transmission in the spectral range between 400 and 1400 nm show very low variation as a function of wavelength compared to variations as a function of mass density. Therefore, we conclude that transmission losses due the deposited dust are largely independent of wavelength and not limited to the spectral region of very high imaginary part of refractive index of the absorbing dust. This may be explained by the fact that strong light absorption by large particles occurs for intermediate values of imaginary refractive index, with less absorption for both very low and very high values. Indeed, transmission averaging with respect to wavelength is equivalent to averaging with respect to size distribution, and hence we observe a near constant total transmission through the spectrum. In terms of theoretical modeling, we show that both two-stream and Monte Carlo methods can model PV module optical efficiency losses for absorbing and non-absorbing dust in good agreement with our experimental results. This agreement is surprising given that our light scattering model (i.e., Mie theory) is relatively primitive and does not model the irregular shape of dust particles. This highlights the overall radiative transfer characteristics of dust layers composed of numerous individual particles as a macroscopic problem rather than a microscopic one for the purposes of modeling dust on PV modules.

## Acknowledgements

This work has been supported in part by the National Science Foundation Solar Energy-Water-Environment Nexus program under the cooperative agreement No. EPS-IIA-1301726. Patricio Piedra acknowledges a Graduate Student Fellowship from NASA-EPSCOR. Very helpful discussions with Drs. W. Patrick Arnott and Christopher M. Sorensen have greatly contributed to the radiative transfer discussion and the comparison with experiments. Dr. Johann P. Engelbrecht has made samples of non-absorbing mineral dust available and Dr. Vicken R. Etyemezian has been essential in motivating and organizing this project. It is also a pleasure to acknowledge helpful discussions with and training by Dr. David E. Rhode on the use of microscopic instruments. We also kindly acknowledge the contribution of Mr. Nicholas D. Beres, who has helped with the development of the experimental apparatus and with discussions on using our laboratory's spectrophotometer.

## References

Al-Hasan, A.Y., 1998. A new correlation for direct beam solar radiation received by photovoltaic panel with sand dust accumulated on its surface. Sol. Energy 63 (5), 323–333.
Andrews, E., Sheridan, P.J., Fiebig, M., McComiskey, A., Ogren, J.A., Arnott, P., Covert, D., Elleman, R., Gasparini, R., Collins, D., Jonsson, H., Schmid, B., Wang, J., 2006. Comparison of methods for deriving aerosol asymmetry parameter. J. Geophys. Res. 111 (D5), 0148–0227.
Bohren, C.F., 1987. Multiple-scattering of light and some of its observable consequences. Am. J. Phys. 55 (6), 524–533.
Bohren, C.F., Clothiaux, E.E., 2006. Fundamentals of Atmospheric Radiation: An Introduction With 400 Problems. John Wiley & Sons.
Bohren, C.F., Huffman, D.R., 1983. Absorption and Scattering of Light by Small Particles. Wiley, New York.
Chylek, P., Wong, J., 1995. Effect of absorbing aerosols on global radiation budget. Geophys. Res. Lett. 22 (8), 929–931.
Costa, S.C.S., Diniz, A.S.A.C., Kazmerski, L.L., 2017. Solar energy dust and soiling R&D progress: literature review update for 2016. Renew. Sustain. Energy Rev. http://dx.doi.org/10.1016/j.rser.2017.1009.1015. (in press).
Engelbrecht, J.P., Moosmüller, H., Pincock, S., Jayanty, R.K.M., Lersch, T., Casuccio, G., 2016. Technical note: mineralogical, chemical, morphological, and optical interrelationships of mineral dust re-suspensions. Atmos. Chem. Phys. 16 (17), 10809–10830.
Etyemezian, V., Nikolich, G., Gillies, J.A., 2017. Mean flow through utility scale solar facilities and preliminary insights on dust impacts. J. Wind Eng. Ind. Aerodyn. 162, 45–56.
Fiebig, M., Ogren, J.A., 2006. Retrieval and climatology of the aerosol asymmetry parameter in the NOAA aerosol monitoring network. J. Geophys. Res. 111(D21), n/a-n/a, http://dx.doi.org/10.1029/2005jd006545.
Fu, R., Feldman, D.J., Margolis, R.M., Woodhouse, M.A., Ardani, K.B., 2017. US Solar Photovoltaic System Cost Benchmark: Q1 2017. National Renewable Energy Laboratory (NREL), Golden, CO (United States).
Gholami, A., Saboonchi, A., Alemrajabi, A.A., 2017. Experimental study of factors affecting dust accumulation and their effects on the transmission coefficient of glass for solar applications. Renew. Energy 112(Suppl. C), 466–473.
Hassan, T., Moosmüller, H., Chung, C.E., 2015. Coefficients of an analytical aerosol forcing equation determined with a Monte-Carlo radiation model. J. Quant. Spectrosc. Radiat. Transfer 164, 129–136.
Hegazy, A.A., 2001. Effect of dust accumulation on solar transmittance through glass covers of plate-type collectors. Renew. Energy 22 (4), 525–540.
Henyey, L.G., Greenstein, J.L., 1941. Diffuse radiation in the galaxy. Astrophys. J. 93, 70–83.
Inman, R.H., Pedro, H.T.C., Coimbra, C.F.M., 2013. Solar forecasting methods for renewable energy integration. Prog. Energy Combust. Sci. 39 (6), 535–576.
Javed, W., Wubulikasimu, Y., Figgis, B., Guo, B., 2017. Characterization of dust accumulated on photovoltaic panels in Doha, Qatar. Sol. Energy 142(Suppl. C), 123–135.
Joseph, J.H., Wiscombe, W., Weinman, J., 1976. The delta-Eddington approximation for radiative flux transfer. J. Atmos. Sci. 33 (12), 2452–2459.
Kaiser, H., 2012. Python translation of mie scattering code in fortran. < http://scatterlib.wikidot.com/mie > .
Kaskaoutis, D.G., Kambezidis, H.D., 2009. The diffuse-to-global and diffuse-to-direct-beam spectral irradiance ratios as turbidity indexes in an urban environment. J. Atmos. Sol. Terr. Phys. 71 (2), 246–256.
Liou, K.-N., 2002. An Introduction to Atmospheric Radiation. Academic Press.
Liu, L., Mishchenko, M.I., Patrick Arnott, W., 2008. A study of radiative properties of fractal soot aggregates using the superposition T-matrix method. J. Quant. Spectrosc. Radiat. Transfer 109 (15), 2656–2663.
Mackowski, D.W., 2010. A generalization of image theory to predict the interaction of multipole fields with plane surfaces. J. Quant. Spectrosc. Radiat. Transfer 111 (5), 802–809.
Maghami, M.R., Hizam, H., Gomes, C., Radzi, M.A., Rezadad, M.I., Hajighorbani, S., 2016. Power loss due to soiling on solar panel: a review. Renew. Sustain. Energy Rev. 59(Suppl. C), 1307–1316.
Mani, M., Pillai, R., 2010. Impact of dust on solar photovoltaic (PV) performance: research status, challenges and recommendations. Renew. Sustain. Energy Rev. 14 (9), 3124–3131.
Meador, W., Weaver, W., 1980. Two-stream approximations to radiative transfer in planetary atmospheres: a unified description of existing methods and a new improvement. J. Atmos. Sci. 37 (3), 630–643.
Metropolis, N., Ulam, S., 1949. The Monte Carlo method. J. Am. Stat. Assoc. 44 (247), 335–341.
Mie, G., 1908. Beiträge zur Optik trüber Medien, speziell kolloidaler Metallösungen. Ann. Phys. 330 (3), 377–445.
Mishchenko, M.I., Travis, L.D., Kahn, R.A., West, R.A., 1997. Modeling phase functions for dustlike tropospheric aerosols using a shape mixture of randomly oriented polydisperse spheroids. J. Geophys. Res.: Atmos. 102 (D14), 16831–16847.
Mishchenko, M.I., Videen, G., Babenko, V.A., Khlebtsov, N.G., Wriedt, T., 2007. Comprehensive T-matrix reference database: a 2004–06 update. J. Quant. Spectrosc. Radiat. Transfer 106 (1), 304–324.
Moosmüller, H., Arnott, W.P., 2003. Angular truncation errors in integrating nephelometry. Rev. Sci. Instrum. 74 (7), 3492–3501.
Moosmüller, H., Chakrabarty, R.K., Arnott, W.P., 2009. Aerosol light absorption and its measurement: a review. J. Quant. Spectrosc. Radiat. Transfer 110 (11), 844–878.
Moosmüller, H., Engelbrecht, J.P., Skiba, M., Frey, G., Chakrabarty, R.K., Arnott, W.P.,

2012. Single scattering albedo of fine mineral dust aerosols controlled by iron concentration. Journal of Geophysical Research. Atmospheres 117(11).
Moosmüller, H., Ogren, J.A., 2017. Parameterization of the aerosol upscatter fraction as function of the backscatter fraction and their relationships to the asymmetry parameter for radiative transfer calculations. Atmosphere 8 (8), 133.
Moosmüller, H., Sorensen, C.M., 2018. Small and large particle limits of single scattering albedo for homogeneous, spherical particles. J. Quantitative Spectrosc. Radiative Transfer 204, 250–255.
Padera, F., 2013. Measuring absorptance (k) and refractive Index (n) of thin films with the PerkinElmer lambda 950/1050 high performance UV-Vis/NIR spectrometers. PerkinElmer Inc.: Application note: UV/Vis Spectroscopy.
Petty, G.W., 2006. A First Course in Atmospheric Radiation. Sundog Pub.
Piedra, P.G., 2014. A Theoretical Calculation of the Polarization of Scattered Ligth and a Comparison with AERONET Measurements: Possible Applications to Aerosol Discrimination. San Jose State University Master's Theses. Paper 4510, San Jose.
Piedra, P.G., Moosmüller, H., 2017. Optical losses of photovoltaic cells due to aerosol deposition: role of particle refractive index and size. Sol. Energy 155, 637–646.
Prahl, S.A., Keijzer, M., Jacques, S.L., Welch, A.J., 1989. A Monte Carlo model of light propagation in tissue. Dosimetry Laser Radiat. Med. Biol. 5, 102–111.
Querry, M.R., 1985. Optical Constants. University of Missouri, Kansas City, DTIC Document.
Said, S.A.M., Walwil, H.M., 2014. Fundamental studies on dust fouling effects on PV module performance. Sol. Energy 107(Suppl. C), 328–337.
Sayyah, A., Horenstein, M.N., Mazumder, M.K., 2014. Energy yield loss caused by dust deposition on photovoltaic panels. Sol. Energy 107, 576–604.
Sobolev, V.V., 1975. Light scattering in planetary atmospheres. (Translation of Rasseianie sveta v atmosferakh planet, Moscow, Izdatel'stvo Nauka, 1972.) Oxford and New York, Pergamon Press (International Series of Monographs in Natural Philosophy. Volume 76), 1975. 263 p.
Sulaiman, S.A., Singh, A.K., Mokhtar, M.M.M., Bou-Rabee, M.A., 2014. Influence of dirt accumulation on performance of PV panels. Energy Procedia 50, 50–56.
Sun, K., Lu, L., Jiang, Y., Wang, Y., Zhou, K., He, Z., 2017. Integrated effects of PM2.5 deposition, module surface conditions and nanocoatings on solar PV surface glass transmittance. Renew. Sustain. Energy Rev.
Videen, G., Ngo, D., 1997. Light scattering from a cylinder near a plane interface: theory and comparison with experimental data. J. Opt. Soc. America A 14 (1), 70–78.
Videen, G., Pinnick, R.G., Ngo, D., Fu, Q., Chýlek, P., 1998. Asymmetry parameter and aggregate particles. Appl. Opt. 37 (6), 1104.
Wang, G., Chakrabarti, A., Sorensen, C.M., 2015. Effect of the imaginary part of the refractive index on light scattering by spheres. J. Opt. Soc. America A 32 (7), 1231–1235.
Wang, L., Jacques, S.L., Zheng, L., 1995. MCML—Monte Carlo modeling of light transport in multi-layered tissues. Comput. Methods Programs Biomed. 47 (2), 131–146.
Wiscombe, W., 1977. The Delta–M method: rapid yet accurate radiative flux calculations for strongly asymmetric phase functions. J. Atmos. Sci. 34 (9), 1408–1422.
Xu, R., Ni, K., Hu, Y., Si, J., Wen, H., Yu, D., 2017. Analysis of the optimum tilt angle for a soiled PV panel. Energy Convers. Manage. 148(Suppl. C), 100–109.
Yurkin, M.A., Hoekstra, A.G., 2011. The discrete-dipole-approximation code ADDA: capabilities and known limitations. J. Quant. Spectrosc. Radiat. Transfer 112 (13), 2234–2247.
Yurkin, M.A., Huntemann, M., 2015. Rigorous and fast discrete dipole approximation for particles near a plane interface. J. Phys. Chem. C 119 (52), 29088–29094.
Zorrilla-Casanova, J., Piliougine, M., Carretero, J., Bernaola-Galván, P., Carpena, P., Mora-López, L., Sidrach-de-Cardona, M., 2013. Losses produced by soiling in the incoming radiation to photovoltaic modules. Prog. Photovoltaics Res. Appl. 21 (4), 790–796.